Archives of Civil and Mechanical Engineering (2023) 23:192
https://doi.org/10.1007/s43452-023-00723-6

ORIGINAL ARTICLE

A cost-effective stereo camera-based system for measuring crack propagation in fibre-reinforced concrete

Álvaro Mena-Alonso[1] · Pedro Latorre-Carmona[2] · Dorys C. González[1] · José F. Díez-Pastor[2] · Juan J. Rodríguez[2] · Jesús Mínguez[1] · Miguel A. Vicente[1]

Received: 15 October 2022 / Revised: 7 June 2023 / Accepted: 17 June 2023 / Published online: 9 July 2023

Abstract
This paper shows a new low-cost technology for the measurement of crack propagation in quasi-fragile materials based on a stereo pair of cameras and LED light spots. The two cameras record the displacement experienced by a series of LED white lights. For each frame, the *X*, *Y* and *Z* 3D coordinates of all the centroids of the LED points are obtained. From this information, it is possible to determine the variation of the distance between any two of them. In this case, 2 strips of 12 LED lights each were arranged in such a way that the points of both strips coincided in pairs in height. The algorithm made it possible to monitor the increase in distance that occurred between each pair of lights at the same height. The paper shows the mathematical basis of this technological solution. A test has been carried out by installing this system in a concrete cube 150 mm side and subjected to a wedge-splitting test. The results show that it is possible to monitor the crack propagation (position of the crack front) during the test and to know the crack width too. At present, the accuracy of this technique is only limited by the camera resolution and the computer processing capability.

Keywords 3D stereo system · Crack propagation · Steel fibre-reinforced concrete · LED lights

1 Introduction

From a scientific point of view, it is very important to accurately measure and evaluate the cracking mechanisms of quasi-fragile materials, such as concrete, mortar or masonry, as a basis for understanding and predicting them [1–3]. Most fracture models are based on characteristic crack parameters such as length and opening. In addition, in recent years, there has been growing interest in the development of fracture mechanics models for non-conventionally reinforced concrete [4–7], such as fibre-reinforced concrete (metallic or non-metallic) and textile-reinforced concrete. Therefore, for the development and validation of robust models, it is essential to measure surface cracks continuously and with sufficient accuracy.

Nevertheless, this is not a simple task. There are a few methods for monitoring crack propagation in concrete and other quasi-fragile materials nowadays [8]. In general, all of them can be classified into three main groups: (a) manual inspection, (b) traditional sensor-based approaches, and (c) image analysis-based methods.

Manual methods mainly consist of visual inspection of structures. Technicians rely on sketches of cracking patterns to determine the origin of cracks and their severity. In addition, simple tools such as crack width comparators or crack gauges are often used. Due to their simplicity and low cost, these methods are the most widely used in structural maintenance programmes. However, they have a serious drawback: their inherent subjective nature. The result of the inspection depends on the knowledge and experience of the specialist, and therefore the structural health of the same element can change depending on who is analysing it. Hence, they are not recommended for quantitative analysis [2].

Crack propagation in concrete can also be monitored with traditional sensors, such as strain gauges. The strain gauge method (SGM) consists of placing gauges with a given orientation along the predicted crack path. When the crack passes close to a strain gauge, a decrease in the

✉ Dorys C. González
dgonzalez@ubu.es

[1] Department of Civil Engineering, Universidad de Burgos, C. Villadiego s/n, 09001 Burgos, Spain

[2] Department of Computer Engineering, Universidad de Burgos, Avda. Cantabria s/n, 09006 Burgos, Spain

measured strain occurs. With this method, it is possible to determine not only crack propagation, but also other parameters related to the fracture mechanics of concrete [9, 10]. In addition, specific strain gauges are available to determine crack propagation. They consist of a set of isolated circuits that are interrupted as the crack propagates [8, 11]. Other sensors are capable of measuring crack width at specific points, such as clip-on strain gauges or displacement transducers. In addition, there are other methods to measure crack propagation, such as those based on accelerometers [12], acoustic emission [13, 14] or embedded piezoelectric transducers [15].

In contrast to visual inspection techniques, traditional sensors provide robust quantitative measurements, making it possible to objectively study the evolution of the structural state of an element. However, these methods require expensive equipment (sensors, data acquisition system, data processing software). Moreover, sensors can only monitor cracks at discrete points. It is, therefore, necessary to estimate the crack trajectory beforehand, which is not always successful.

In the last decade, methods based on image analysis have reached a high level of development, with numerous papers demonstrating their potential application for the measurement of cracking in concrete [2, 3]. As detailed in Mohan and Poobal [3], the general process of image analysis techniques for crack detection consists of the following steps: (1) acquisition of images of the structure to be monitored. (2) Pre-processing of the images to optimise further processing. Typically, these techniques consist of image segmentation and/or binarization. (3) Image processing using one of the image analysis techniques. As a result, the cracks are detected and their main parameters, such as length, opening and propagation direction, are obtained.

Image analysis comprises a wide range of techniques. Amongst those that have attracted most scientific interest for concrete crack monitoring are digital image processing (DIP) [1, 16, 17], digital image correlation (DIC) [18–21] and machine vision [22–24], amongst others. In all these cases, a set of cameras capture a sequence of images over time, which are analysed. The comparison between images can be carried out in different ways. In some cases, prior to the start of the test, a series of dots (e.g. small paint droplets) are drawn on the surface of the specimen, and the algorithm identifies each of the dots and their spatial variation over time. From the information of the absolute and relative movements of each of the dots, it is possible to develop deformation maps and to identify where the crack runs.

In other cases, it is the texture of the surface (and its different colours and/or shades) which serves as a basis for evaluating the variation of the surface over time. Generally, cracks are identified as lines that are darker than the rest of the surface (especially when the surface is naturally or artificially illuminated). Finally, the algorithm identifies and isolates the cracks.

Their main advantage is their low cost compared to traditional sensors, as they can monitor the movement of a huge amount of points simultaneously. In addition, they are not limited by a measurement range and do not need to be placed exactly in the path of the cracks, giving them more room for manoeuvre than traditional sensors. Finally, they are not invasive, as the system is not in contact with the element (although the speckles and, sometimes, the reference points such as stickers, are placed on the element) [25].

This paper proposes a novel machine vision-based solution for monitoring crack propagation in concrete. The system consists of two elements. On the one hand, a stereo camera pair formed by commercially available digital video cameras, which records the surface of the concrete element to be monitored. On the other hand, two LED strips placed in parallel on both sides of the expected trajectory of the crack. The captured images are post-processed with an algorithm developed by the authors and implemented in MATLAB (MathWorks, Natick, MA, USA).

Here, the main difference with the methods based on image analysis previously mentioned is that the reference points are light emitters. This system makes it possible to measure the crack opening, not at a single point, but along a line. This is done by monitoring the 3D relative distance between the pairs of LED lights on either side of the crack. This is, therefore, a very cost-effective solution, as the relative movement of many points can be monitored with a single device. Another added advantage is that it can operate under any lighting conditions, as the reference points are LEDs. This is especially important in some applications, such as long-term tests that can last for days or months.

In this paper, a case of application of the system is described, consisting of a fibre-reinforced concrete cube subjected to a wedge-splitting test. The paper is structured as follows. The test setup is described in Sect. 2. The calibration process of the stereo camera is detailed in Sect. 3. The experimental results and the technological possibilities of the solution are presented in Sect. 4. Finally, the conclusions are presented in Sect. 5.

2 Experimental setup

A prism was cast to perform this work. The specimen dimensions were 150 mm in height, 150 mm in width and 600 mm in length. In this case, steel fibre-reinforced concrete was used. Table 1 shows the mix proportion.

Table 1 Mix proportion

Materials (kg/m^3)	Mix proportion
Cement	400.0
Fine aggregate	800.0
Coarse aggregate	1080.0
Nano silica	6.0
Water	125.0
Superplasticizer	14.0
Fibres	150.0

The fibres used were Dramix 3D 55/60 BG (BEKAERT, Kortrijk, Belgium), 60 mm in length and 1.05 mm in thickness. The volume of the fibre fraction was around 2% in volume. MasterGlenium 51 superplasticizer (BASF, Ludwigshafen, Germany) and MasterRoc MS 685 nano-silica (BASF, Ludwigshafen, Germany) were used, as well as CEM I 52.5 R Portland cement. The characteristic concrete compression strength was 69.6 MPa.

Once the concrete prism has reached sufficient strength to withstand a disc-cutting operation, one cube 150 mm side was extracted from the central part of the prism. The cube was then prepared by sawing a groove and a notch on one side (Fig. 1). In this case, the groove and the notch were cut on the top face along the transverse axis of the prism.

A wedge-splitting test was performed, as characterised by Brühwiler and Wittmann [26]. During the test, the following parameters were measured: applied load and the crack opening displacement (COD). A tension–compression MTS 244.21 dynamic actuator (MTS, Eden Prairie, MN, USA) was used, with a capacity of ± 50 kN. The actuator has a load cell MTS 661.20F-02 with a range of ± 50 kN and an error of below 1% of the range.

During the test, a vertical load was applied, the displacement was controlled, and the test speed was 0.05 mm/min until reaching the maximum load, followed by a speed of 0.2 mm/min. The vertical force could be disaggregated at roller level into two forces: a vertical and a horizontal one. Interested readers can find full details of this type of test in González et al. [27].

The concrete cube has a series of 12 parallel white LEDs couples attached to it. A system formed by two cameras (creating a stereo pair) points directly and perpendicularly towards the front face of the specimen on which the LEDs are placed. Both cameras are Logitech Brio (Logitech, Lausanne, Switzerland), capable of 4 K resolution (4096 × 2160 pixels) and a frame rate of 30 fps. In addition, laser distance sensors are also used in this test to measure the COD, as a contrast measurement to validate the robustness of the new stereo camera-based system. These are high-precision laser distance sensors manufactured by Wenglor (Tettnang, Germany), with a measuring range of 50 mm and an accuracy of 0.01 mm (Figs. 2, 3).

Figures 4 and 5 show, in detail, the 12 pairs of LED lights arranged in the test tube. On both sides of the concrete specimen, a series of 2 LED strips were glued, with 12 lights each. Both strips were vertically oriented and parallel between them, so that two different LEDs were horizontally coincident (that is, at the same height). The result for the image analysis methodology is the assessment of the 3D spatial coordinates (X, Y, Z) of each one of the 24 LEDs, L_1 to L_{12} and R_1 to R_{12}. L_i and R_i, $i = 1$ to 12. In addition, two small L-shaped metal pieces are attached to the cube. On them are the points, R_0 and L_0, whose displacement is measured with laser distance sensors.

As can be observed, these are placed in such a way that, during the test, the crack runs inside the pairs of LED lights.

One of the main advantages this solution offers is that it is possible to measure the distance between any pair of points as long as they are within the field of view of the camera pair.

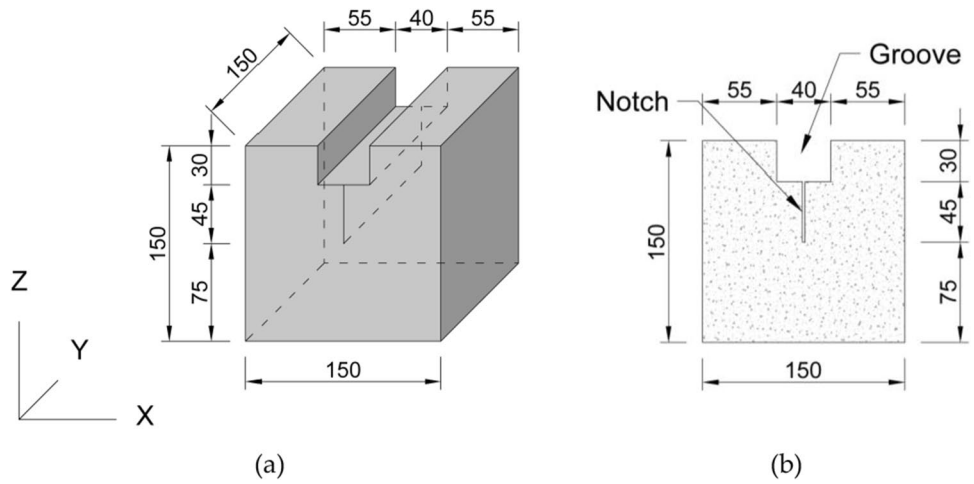

Fig. 1 Geometry of the cubic specimen. **a** 3D view and **b** cross-section

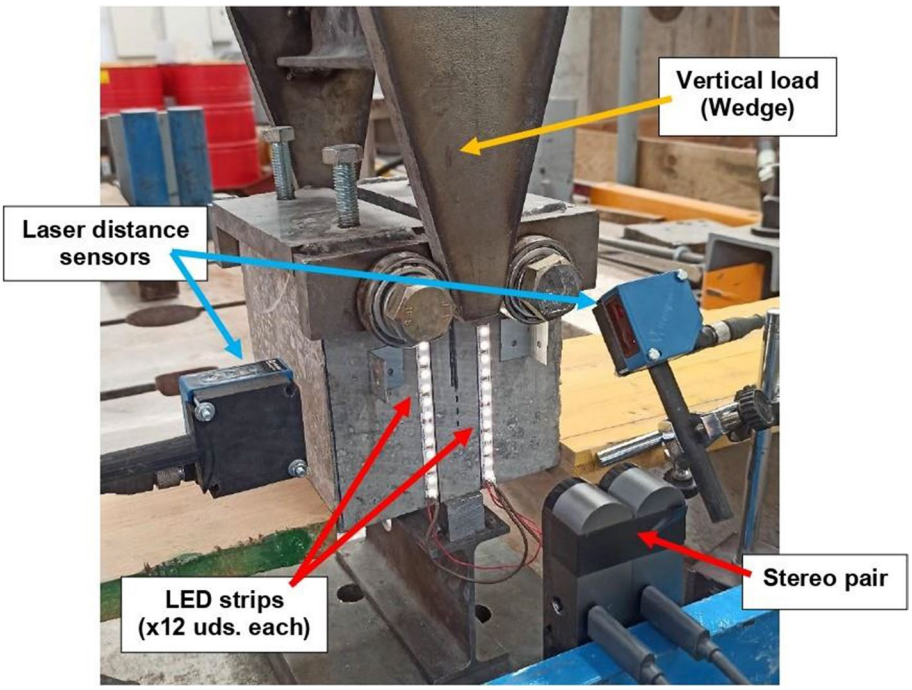

Fig. 2 Experimental device. The stereo pair points at the face of the concrete specimen where two LED strips are placed. This system is able to measure the 3D distance between all pairs of LEDs. Simultaneously, two laser distance sensors measure the COD, taking two metallic plates as a reference

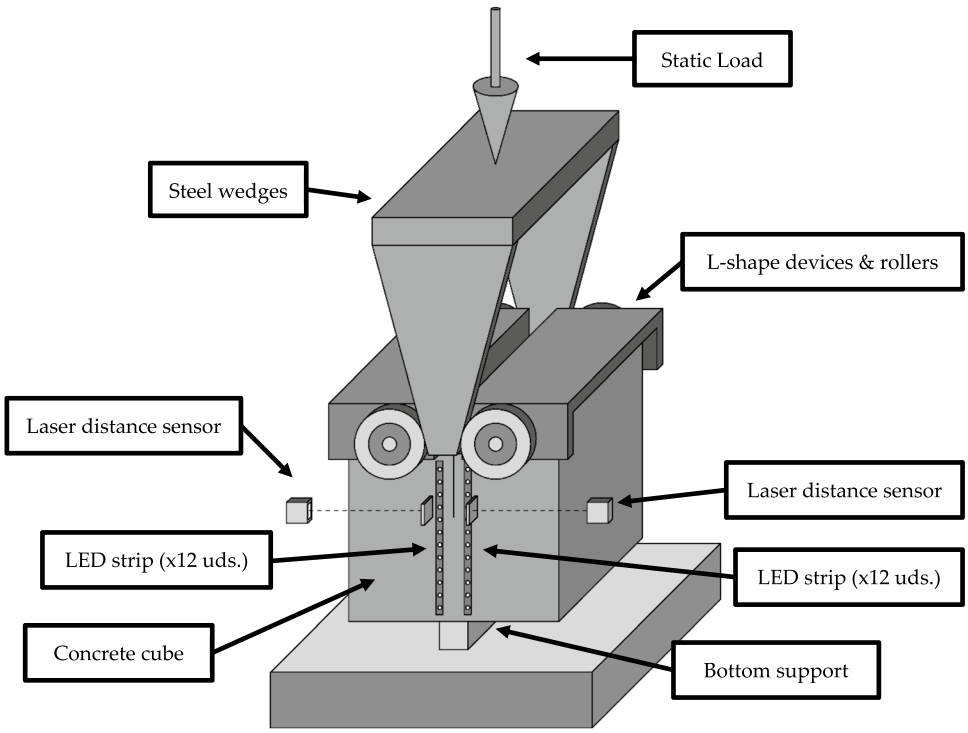

Fig. 3 Scheme of the WST. General view

Therefore, for a series of j frames in a video acquired during the test, each position pair $L_{ij}, R_{ij} (1 \leq i \leq 12)$ defines a reading position $C_{ij} (1 \leq i \leq 12)$. Crack opening for each one of the reading positions for frame j is given by the difference between the L_{ij} and R_{ij} points in that image, and the corresponding positions in the first video image (that we name as $j = 0$), i.e. (Eq. 1):

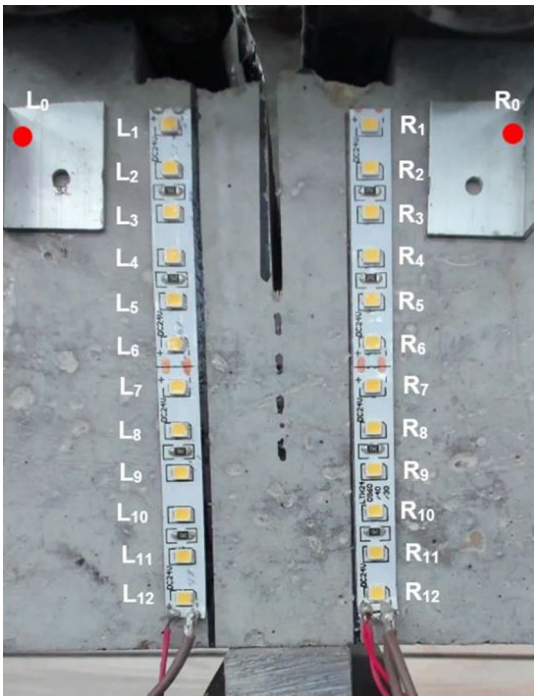

Fig. 4 Picture of the distribution of the 24 light points (12 on the left, R_1 to R_{12} and 12 on the right, L_1 to L_{12}) and the corresponding measurement points for the laser-based distance measurement system (R_0 and L_0)

$$C_{ij} = \sqrt{\left(X_{L_{ij}} - X_{R_{ij}}\right)^2 + \left(Y_{L_{ij}} - Y_{R_{ij}}\right)^2 + \left(Z_{L_{ij}} - Z_{R_{ij}}\right)^2} - \sqrt{\left(X_{L_{i0}} - X_{R_{i0}}\right)^2 + \left(Y_{L_{i0}} - Y_{R_{i0}}\right)^2 + \left(Z_{L_{i0}} - Z_{R_{j0}}\right)^2}. \quad (1)$$

This framework is implicitly assuming that an increase in the distance between L_{ij} and R_{ij} ($1 \le i \le 12$) is only due to the presence of the crack between them, therefore disregarding the elastic deformation that might appear between both points.

Additionally, both laser distance measurement systems are located at both sides of the test specimen and monitor the transverse movements (movements in the X axis, as per our reference system) of L_{0j} and R_{0j}. L_{0j}, R_{0j} pair define the C_{0j} lecture position. The crack opening for this picture position would be given by the difference in the horizontal movements from both points.

3 Camera stereo pair calibration

The use of more than one camera, even an array of cameras, in different geometric or non-geometric types of arrangement, aimed to infer the 3D information of a scene, is an intensively research topic nowadays. The minimum number

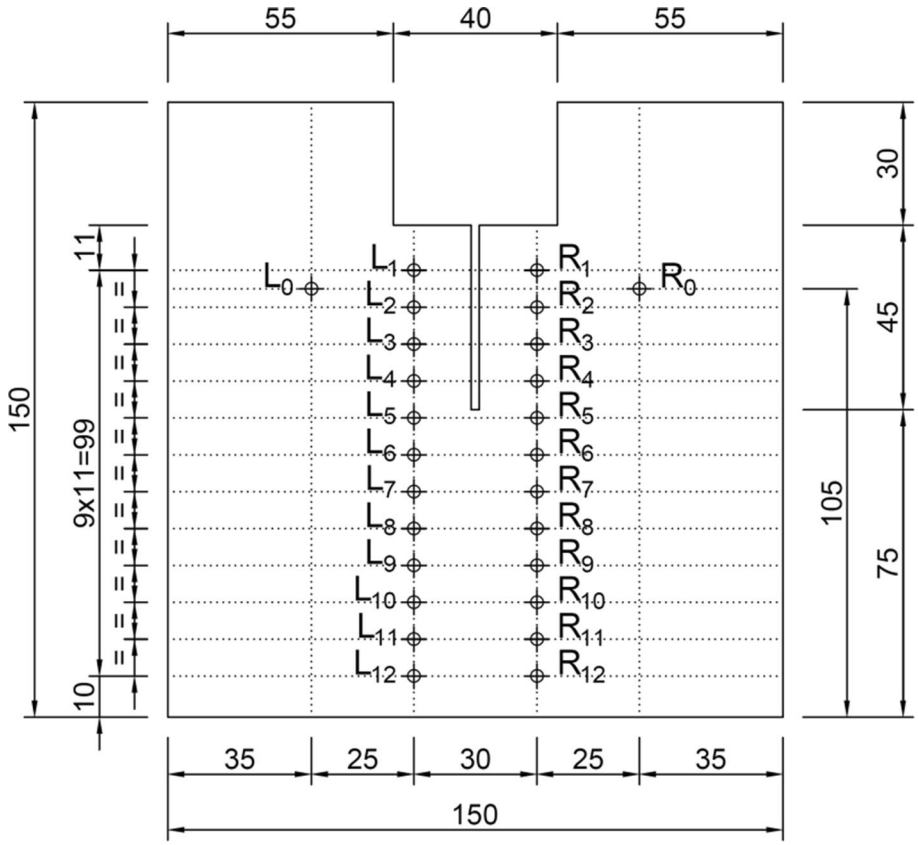

Fig. 5 Position of R_1 to R_{12}, L_1 to L_{12} and R_0 and L_0 (dimensions in mm)

of cameras to be used is two, even though more may be considered, depending on the application, cost and precision we are aiming to [28, 29]. When two cameras are considered, a so-called stereo pair is formed.

In this case, the stereo camera calibration is a process by which we characterise the intrinsic and extrinsic parameters of each one of the cameras, the rotation and translation matrix that transforms one into the other, and the inference of the 3D world coordinates that allow us to obtain the real 3D coordinates of any point in the scene the camera pair acquired the image of.

Single camera calibration is usually obtained by the method presented in Zhang [30]. It is based on the use of a planar checkerboard (rectangular structure formed by black and white squares ordered as a checkerboard) that is presented to each camera in different positions and orientations. It is recommended that at least ten different positions of the checkerboard be used for camera calibration, and all the internal black squares should be fully viewed from each camera. This method uses the identification of all the corner points of the internal squares in the checkerboard images to infer the relationship between the camera pixel (u, v) coordinates and the corresponding 3D (X, Y, Z).

A set of correspondences between 2D points of each one of the images of the camera pair $(x_i \leftrightarrow x_i^{'})$ is considered. For instance, the corner points for the checkerboard, detected by each camera, for each checkerboard position. It is assumed that there exist camera matrices, P and P', and a set of 3D points X_i, so that $PX_i = x_i$ and $P'X_i = x_i'$.

The basic tool in the reconstruction of point sets from two views is the so-called fundamental matrix, which represents the constraint obeyed by image points x and x' if they are to be images of the same 3D point. This constraint arises from the co-planarity of the camera centres of the two views. Given the fundamental matrix, F, a pair of matching points $(x_i \leftrightarrow x_i')$ must satisfy: $x_i^{'T} F x_i = 0$. The fundamental matrix estimation method to obtain the scene coordinates is a well-established method and would consist of the following steps [31]: (a) given several correspondences $(x_i \leftrightarrow x_i')$, find the fundamental matrix that accomplishes: $x_i^{'T} F x_i = 0$; (b) compute the pair of camera matrices (P, P') from F; (c) obtain the 3D coordinates of the X_i points by a triangulation process.

The triangulation process assumes that each point in an image corresponds to a line in 3D space. Therefore, all points on the line in 3D are projected to the point in the image. If a pair of corresponding points in two images can be found, then they should be the projection of a common 3D point X. The set of lines generated by the image points must, therefore, intersect at X.

As stated above, once the calibration is obtained, we can obtain the 3D coordinates that correspond to any pixel position of any of the two images that form the camera pair.

4 Experimental results and discussion

In this section, the details of the camera pair calibration and the results of a case study are presented.

4.1 Stereo camera pair calibration

Twenty-three images of the checkerboard in different positions and orientations were used for the stereo camera calibration. From these image pairs, 18 were finally considered for the calibration (the rest were discarded because not all the corners in the black squares of the checkerboard were identified). Figure 6 shows a 3D view of the camera positions, orientations, and also the different orientations of the checkerboard. Numbers in the checkerboards in this figure are associated to the total number of images.

Figure 7a shows the images acquired by the left and right cameras, for one position of the checkerboard. Figure 7b shows a barplot for the so-called re-projection error (in pixels) for each camera and image used for the calibration. The overall mean error is 1.22, which may be considered as an appropriate value (it should ideally be ≤ 1 pixel).

On the other hand, the calibration model for each camera was applied to the images acquired by them to undistort them. This undistortion process can be obtained because the calibration method also estimated the geometric distortion created by their optical systems.

Left and right undistorted image pairs (Fig. 8a, b) were then used to obtain the so-called disparity map (Fig. 8d). This map infers the displacement in pixels between corresponding points in both images. We used the method

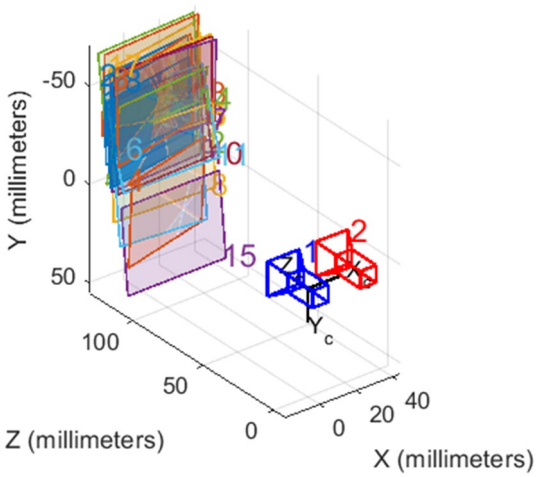

Fig. 6 3D plot showing the location and orientation of the camera stereo pair, as well as the orientation of the checkerboards used for the calibration process, applying the method in Hartley and Zisserman [25]

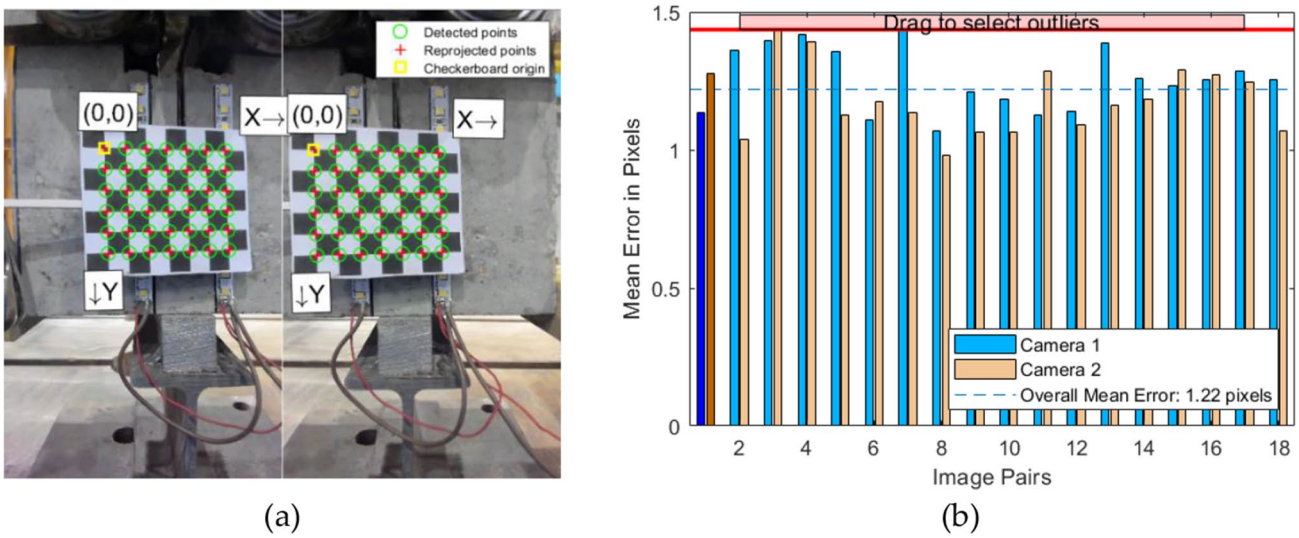

Fig. 7 **a** Identification of re-projected points (as per calibration model) in the checkerboard; **b** re-projection root mean squared error (RMSE) for each pair of calibration images

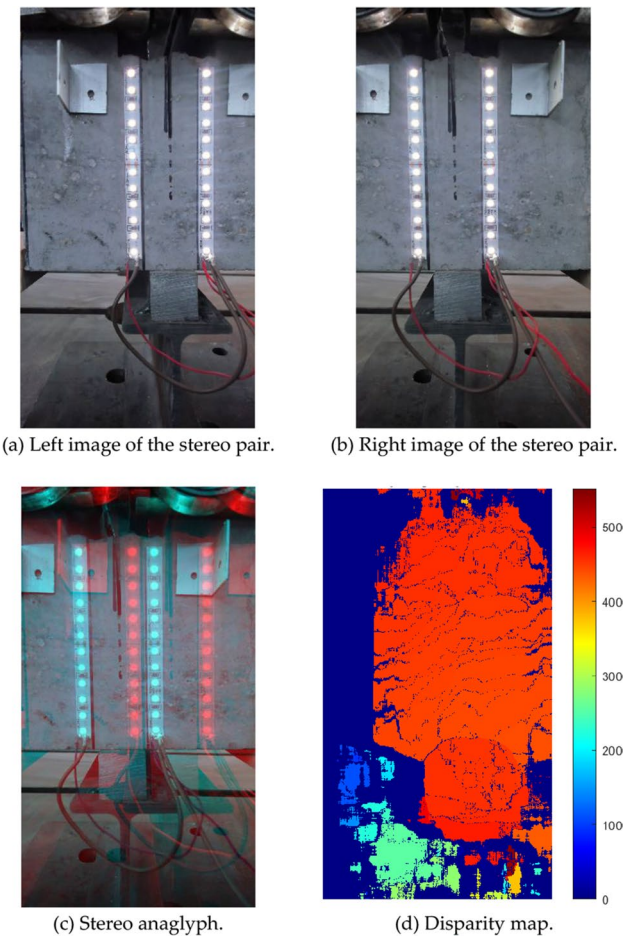

(a) Left image of the stereo pair. (b) Right image of the stereo pair.

(c) Stereo anaglyph. (d) Disparity map.

Fig. 8 Stereo pair, anaglyph and disparity map image for the frame corresponding to second number 10

proposed in Gonzalez-Huitron et al. [32] to compute it, using the so-called sum of absolute differences (SAD) criterion between blocks of pixels. These blocks are used to find correspondences between images. A 551×551 pixels block was used in our case. An anaglyph of the pair of images is shown in Fig. 8c.

Once a robust disparity map is obtained, the stereo calibration parameters structure is applied to infer the 3D coordinates that correspond to the 2D pixel coordinates for each camera image. Figure 9 shows the 3D *XYZ* physical coordinates of each pixel RGB value has for an image before and after breaking up (a frame of the video frame in the second 10th of the experiment, and a frame just before the end of the video, which lasts for 16 min and 34 s).

4.2 Crack measurement

Measuring the 3D real distance between each pair of LED centroids (L_i and R_i) as a function of time would allow to analyse the temporal evolution of the crack when propagating throughout the concrete prism.

To infer the distance between each $\left(L_i, R_i\right)$ pair, a mask was first created with the shape of each LED. This was made by identifying those pixels in each image whose colour coordinates$(R, G, B) \geq (235, 235, 235)$. A mask was created from this identification in such a way that those pixels accomplishing this inequality were given a value of 1, and 0 otherwise. From this mask, the centroid of each LED was inferred.

Figure 10a shows (in red) the pixels that are identified as LED pixels in the image. Figure 10b shows the corresponding mask, as well as the centroid of each LED (with a green

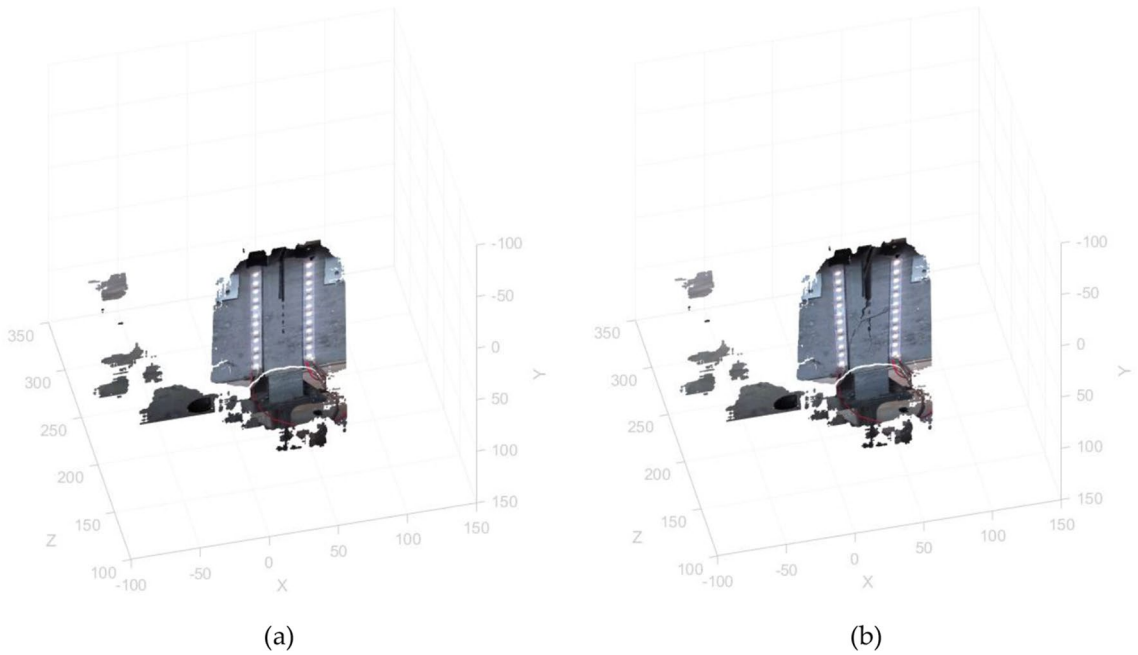

Fig. 9 3D visualisations corresponding to the 3D pixels of the image for the left camera of the stereo pair for: **a** frame after 10 s, and **b** frame after 16 min and 34 s

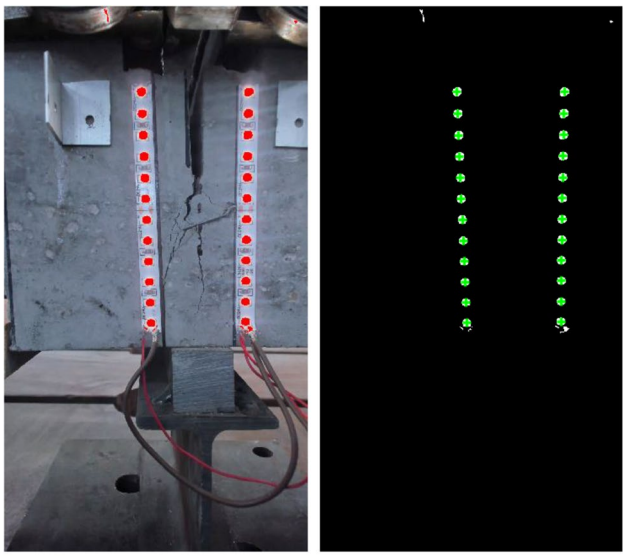

Fig. 10 **a** Image processing to identify the pixels in the image that belong to each LED. **b** Mask and centroid of each LED in the image. This image corresponds to the case where the crack was completely developed, and the loading test had finished

cross each). For each one of these centroid coordinates, i.e. (u_{L_i}, v_{L_i}) or (u_{R_i}, v_{R_i}), we obtain the corresponding 3D coordinates, i.e. $(X_{L_i}, Y_{L_i}, Z_{L_i})$ or $(X_{R_i}, Y_{R_i}, Z_{R_i})$, and from them, the Euclidean distance accordingly.

Figure 11 shows the distance between the centroids for the 12 pairs of LEDs (that is, the COD as a measure characterising the evolution of the crack in the concrete structure), as a function of time, as given by the camera stereo pair, and the distance change between metallic plates, as measured by the laser distance measurement sensors.

First of all, it should be noted that the results obtained, in terms of the study of the mechanical properties of concrete, in general, are of minor value, since only one test specimen has been tested. The interest of this test is focussed on the assessment of the technological possibilities offered by the solution presented here. In this case, the concrete specimen is only a support to evaluate the potential of the system for movement monitoring based on artificial vision.

Figure 11 reveals that all curves have an increasing trend with time (i.e. throughout the test). The measurements are perfectly ordered according to their position. It is satisfied that$C_i > C_{i+1} (1 \leq i \leq 11)$, i.e. the higher the reading position, the larger the crack opening. The position curve C_0 lies approximately between the position curves C_1 and C_2, which makes sense since, geometrically, it lies between the two.

It should be noted that, although the test is performed at constant displacement speed (i.e. constant opening speed of the thrust rollers), the crack opening at all positions does not follow a straight line, but a second degree parabola. In particular, a very good fit has been obtained for parabolas of the form $\mathrm{COD} = A \cdot t^2 - B \cdot t (t \geq 0)$, where A and B are two constants depending on the reading position. Table 2 shows

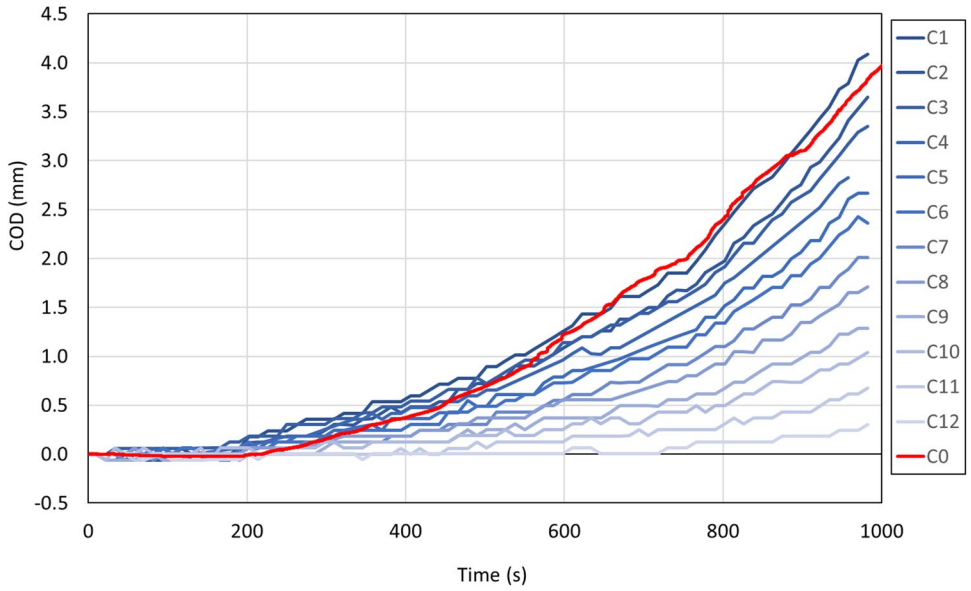

Fig. 11 Variation of the crack opening displacement over time, measured in the different reading positions

Table 2 A, B and R^2 values

Reading position	A (mm/s^2)	B (mm/s)	R^2	B/A (s)
C_1	4.5×10^{-6}	5.6×10^{-4}	0.991	124.4
C_2	4.2×10^{-6}	7.1×10^{-4}	0.992	169.0
C_3	3.5×10^{-6}	2.2×10^{-4}	0.991	62.9
C_4	3.3×10^{-6}	3.3×10^{-4}	0.992	100.0
C_5	3.1×10^{-6}	5.2×10^{-4}	0.990	167.7
C_6	2.8×10^{-6}	4.5×10^{-4}	0.991	160.7
C_7	2.6×10^{-6}	6.2×10^{-4}	0.994	238.5
C_8	2.0×10^{-6}	3.2×10^{-4}	0.990	160.0
C_9	1.5×10^{-6}	3.0×10^{-4}	0.985	200.0
C_{10}	1×10^{-6}	1.1×10^{-4}	0.965	110.0
C_{11}	9×10^{-7}	3.0×10^{-4}	0.971	333.3
C_{12}	5×10^{-7}	2.5×10^{-4}	0.869	500.0
C_0	5×10^{-6}	1.0×10^{-3}	0.999	200.0

the values of these constants for the different reading positions, as well as the correlation coefficient of the fit.

Parabolas of the form $A \cdot t^2 - B \cdot t$ cut the abscissa axis at two points, namely 0 and B/A. Between $t=0$ and $t = B/A$, the function takes negative values, and for $t > B/A$, it takes positive values. From the experimental point of view, this means that each reading position shows, throughout the test, two stages with different behaviour. Initially (between $t=0$ and $t = B/A$ seconds), the COD value is negative, which means that there is no crack crossing that reading position. From the instant $t = B/A$ onwards, the COD value is positive, and therefore the crack has crossed that reading position already. Table 2 shows the value of B/A, i.e. the time instant from which the crack appears.

Figure 12 shows the B/A values for the different reading positions, i.e. the time instant at which the crack crosses through them. In this figure, two relevant reading positions can be highlighted. The first one is C_0, which is the one corresponding to the laser distance measurement systems. This reading position indicates that the crack appears 200 s after the start of the test. The second important reading position is C_5, since the crack starts at the end of the notch, i.e. approximately at this position. This reading position detects the crack passage at 167.7 s. Therefore, it can be deduced that the crack appears at around 160–170 s. There are reading positions that "detect" the crack earlier than position C_5, which does not make physical sense and can be explained because of the intrinsic error of the measurement system, and of the parabolic adjustment itself. Between positions C_0 and C_{10} the crack passage times are similar, and no trend is observed. A different situation occurs with positions C_{11} and C_{12}, where a marked increase in the crack passage time is observed.

It is concluded that, in this case, the crack was born approximately 170 s after the beginning of the test and that it propagates at high speed up to position C_{10}, slowing down at that position. From this moment on, the growth rate is much slower, taking approximately 160 s to reach position C_{11} and another 160 s to reach position C_{12}.

The accuracy that has been achieved in this application case is 0.05 mm. This is an acceptable value, although worse than that achieved by traditional sensors. The current limitations of this technological solution are due to the quality of the cameras (currently the best cameras record in 4 K, but in the near future 8 K and even better cameras will be available), the capture speed (conventional cameras record at 50 fps, but there are commercial super slow-motion cameras

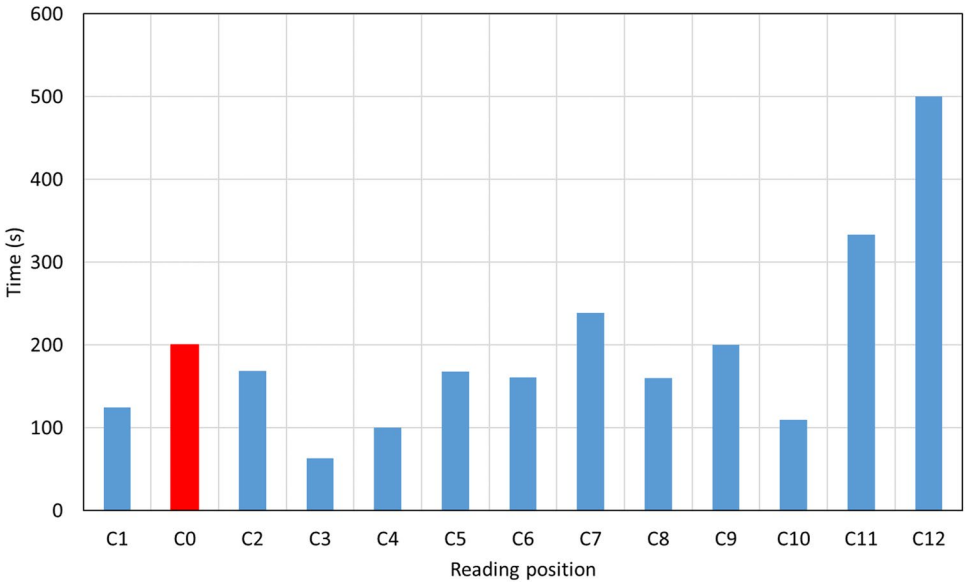

Fig. 12 Time instant at which the crack crosses through the reading position

that can record at up to 1000 fps) and the post-processing capacity of the recording framework. At any rate, the measurement procedure described in this paper is independent of all these technical limitations.

An improvement of the recording quality results directly in a reduction of the pixel size and consequently in an improvement of the accuracy of the solution. Higher readout and post-processing frequency will allow higher propagation velocities to be evaluated more accurately.

5 Conclusion

This paper describes a novel technological solution for the measurement of crack propagation in quasi-fragile materials based on a stereo pair of cameras and LED light spots.

The two cameras record, synchronously, all the control points, which are materialised by LED lights of a single colour (in this case, white LEDs). Using an algorithm developed by the authors in MATLAB, it is possible to obtain, for each frame, the X, Y and Z coordinates of all the centroids of the points of light. From this information, it is possible to determine the variation of the distance between any two points.

In this case, two strips of LED lights were arranged on both sides of the expected cracking path in the test. Each one of these strips had a total of 12 light points and they were arranged in such a way that the points of both strips coincided in pairs in height. The algorithm made it possible to monitor the increase in distance that occurred between each pair of lights, at the same height.

A wedge-splitting test was carried out on a cubic specimen to analyse the technological possibilities of this solution. During the first part of the test, the distance between the two remained approximately constant, until it started to increase. At this point, it is possible to be sure that the crack is passing through this mark. By integrating the information provided by the 12 pairs of lights, it is possible to determine when the crack is passing through each of them, i.e. how the crack is progressing.

The solution makes it possible to multiply very considerably the number of points to be measured at a very low cost and, therefore, to multiply the information that can be obtained. The accuracy provided by the system is around 0.05 mm. An improvement in camera resolution (over and above the current 4 K technology) will allow a reduction in pixel size and, by extension, an increase in accuracy. On the other hand, an increase in camera capture speed and an increase in the post-processing speed of the computer equipment will allow for a more accurate monitoring of the evolution of cracking over time. In any case, the advantage of the solution shown in this article is that it is independent of the technical characteristics of the camera and the post-processing equipment.

The technological solution shown in this paper can easily be extrapolated to the monitoring of real structures. A direct application is the monitoring of the evolution over time of existing cracks in bridges and buildings made of concrete and other quasi-brittle materials. This technology can help bridge maintainers to carry out more efficient surveillance, minimising sudden structural failures and optimising repair costs by avoiding untimely work.

As a non-invasive and cost-competitive solution compared to traditional ones, it could be more easily implemented in real structures to assist in SHM of existing structures.

Funding Open Access funding provided thanks to the CRUE-CSIC agreement with Springer Nature. The authors are grateful for financial support from the Ministerio de Economía y Competitividad, Spain, with grant no. PID2019-110928RB-C32, the Ministerio de Ciencia e Innovación, project PID2020-119894GB-I0, and the Junta de Castilla y León project BU055P20; co-financed through European Union FEDER funds.

Declarations

Conflict of interest Authors declare that they have no conflict of interest in relation to this paper or line of research.

Ethics approval The authors declare that the following is fulfilled: (1) this material is the authors' own original work, which has not been previously published elsewhere. (2) The paper is not currently being considered for publication elsewhere. (3) The paper reflects the authors' own research and analysis in a truthful and complete manner. (4) The paper properly credits the meaningful contributions of co-authors and co-researchers. (5) The results are appropriately placed in the context of prior and existing research. (6) All sources used are properly disclosed (correct citation). Literally copying of text must be indicated as such using quotation marks and giving proper reference. (7) All authors have been personally and actively involved in substantial work leading to the paper, and will take public responsibility for its content.

References

1. Valença J, Puente I, Júlio E, González-Jorge H, Arias-Sánchez P. Assessment of cracks on concrete bridges using image processing supported by laser scanning survey. Constr Build Mater. 2017;146:668–78. https://doi.org/10.1016/j.conbuildmat.2017.04.096.
2. Bayar G, Bilir T. A novel study for the estimation of crack propagation in concrete using machine learning algorithms. Constr Build Mater. 2019;215:670–85. https://doi.org/10.1016/j.conbuildmat.2019.04.227.
3. Mohan A, Poobal S. Crack detection using image processing: a critical review and analysis. Alex Eng J. 2018;57(2):787–98. https://doi.org/10.1016/j.aej.2017.01.020.
4. Zhang Y, Woody Ju J, Xu F, Yan Z, Zhu H. A novel micromechanical model of residual fracture energy of hooked-end steel fiber reinforced concrete exposed to high temperature. Constr Build Mater. 2021;278:122211. https://doi.org/10.1016/j.conbuildmat.2020.122211.
5. Congro M, Sanchez ECM, Roehl D, Marangon E. Fracture modeling of fiber reinforced concrete in a multiscale approach. Compos B Eng. 2019;174(March):106958. https://doi.org/10.1016/j.compositesb.2019.106958.
6. Montero-Chacón F, Cifuentes H, Medina F. Mesoscale characterization of fracture properties of steel fiber-reinforced concrete using a lattice-particle model. Materials. 2017. https://doi.org/10.3390/ma10020207.
7. Bielak J, Li Y, Hegger J, Chudoba R. Numerical and experimental characterization of Anchorage length for textile reinforced concrete. In: Mechtcherine V, Slowik V, Kabele P, editors. Strain-hardening cement-based composites. Springer; 2018. pp. 409–17. https://doi.org/10.1007/978-94-024-1194-2_48.
8. Ju M, Li J, Yao Q, Li X, Zhao J. Rate effect on crack propagation measurement results with crack propagation gauge, digital image correlation, and visual methods. Eng Fract Mech. 2019;219(June):106537. https://doi.org/10.1016/j.engfracmech.2019.106537.
9. Li Q, Gao ZH, Yu Q, Huang C, Wang K, Xu WL. Effect of explosive stress waves on the crack propagation in the defective medium using strain gauge method. KSCE J Civ Eng. 2022;26(6):2780–8. https://doi.org/10.1007/s12205-022-0787-9.
10. Ahmad Aasim B, Khaliq Karimi A, Toimyama J, Suda Y. Horizontal end crack control and load-bearing capacity performance of hollow-type pretensioned girders through experimentally calibrated finite element models. Eng Sci Technol Int J. 2021;24:1262–71.
11. Zhou C, Zhu Z. Study of crack dynamic propagation behavior of fine-grained concrete under static loading. Int J Fract. 2019;220(1):113–25. https://doi.org/10.1007/s10704-019-00394-6.
12. Ahmad Aasim B, Khaliq Karimi A, Toimyama J, Aydan O. Numerical verification of accelerometer-based assessment of hollow-type pretensioned concrete girder. Asian J Civil Eng. 2020;21:437–47.
13. Mhamdi L, Schumacher T, Linzer L. Seismology-based acoustic emission techniques for the monitoring of fracture processes in concrete structures. Acoust Emiss Relat Non Destr Eval Tech Fract Mech Concr. 2015. https://doi.org/10.1016/B978-0-12-822136-5.00005-8.
14. Gollob S, Kocur G, Schumacher T, Mhamdi L, Vogel T. A novel multi-segment path analysis based on a heterogeneous velocity model for the localization of acoustic emission sources in complex propagation media. Ultrasonics. 2017;74:48–61.
15. Dumoulin C, Karaiskos G, Deraemaeker A. Monitoring of crack propagation in reinforced concrete beams using embedded piezoelectric transducers. Acoust Emiss Relat Non Destr Eval Tech Fract Mech Concr. 2015. https://doi.org/10.1016/B978-0-12-822136-5.00008-3.
16. Mazzoli A, Monosi S, Plescia ES. Evaluation of the early-age-shrinkage of fiber reinforced concrete (FRC) using image analysis methods. Constr Build Mater. 2015;101:596–601. https://doi.org/10.1016/j.conbuildmat.2015.10.090.
17. Kanema JM, Eid J, Taibi S. Shrinkage of earth concrete amended with recycled aggregates and superplasticizer: impact on mechanical properties and cracks. Mater Des. 2016;109:378–89. https://doi.org/10.1016/j.matdes.2016.07.025.
18. Fayyad TM, Lees JM. Experimental investigation of crack propagation and crack branching in lightly reinforced concrete beams using digital image correlation. Eng Fract Mech. 2017;182:487–505. https://doi.org/10.1016/j.engfracmech.2017.04.051.
19. Gehri N, Mata-Falcón J, Kaufmann W. Automated crack detection and measurement based on digital image correlation. Constr Build Mater. 2020;256:119383. https://doi.org/10.1016/j.conbuildmat.2020.119383.
20. Hamrat M, Boulekbache B, Chemrouk M, Amziane S. Flexural cracking behavior of normal strength, high strength and high strength fiber concrete beams, using Digital Image Correlation technique. Constr Build Mater. 2016;106:678–92. https://doi.org/10.1016/j.conbuildmat.2015.12.166.

21. Dong W, Rong H, Wu Q, Li J. Investigations on the FPZ evolution of concrete after sustained loading by means of the DIC technique. Constr Build Mater. 2018;188:49–57. https://doi.org/10.1016/j.conbuildmat.2018.08.077.
22. Liu Z, Cao Y, Wang Y, Wang W. Computer vision-based concrete crack detection using U-net fully convolutional networks. Autom Constr. 2019;104(April):129–39. https://doi.org/10.1016/j.autcon.2019.04.005.
23. Kim H, Ahn E, Cho S, Shin M, Sim SH. Comparative analysis of image binarization methods for crack identification in concrete structures. Cem Concr Res. 2017;99(April):53–61. https://doi.org/10.1016/j.cemconres.2017.04.018.
24. Bernstone C, Heyden A. Image analysis for monitoring of crack growth in hydropower concrete structures. Measurement. 2009;42(6):878–93. https://doi.org/10.1016/j.measurement.2009.01.007.
25. Gehi N, Mata-Falcon J, Kaufmann W. Automated crack detection and measurement based on digital image correlation. Constr Build Mater. 2020;256:119383.
26. Brühwiler E, Wittmann FH. The wedge splitting test, a new method of performing stable fracture mechanics tests. Eng Fract Mech. 1990;35(1–3):117–25. https://doi.org/10.1016/0013-7944(90)90189-N.
27. González DC, Mínguez J, Vicente MA, Cambronero F, Aragón G. Study of the effect of the fibers' orientation on the post-cracking behavior of steel fiber reinforced concrete from wedge-splitting tests and computed tomography scanning. Constr Build Mater. 2018;192:110–22. https://doi.org/10.1016/j.conbuildmat.2018.10.104.
28. Seitz SM, Curless B, Diebel J, Scharstein D, Szeliski R. A comparison and evaluation of multi-view stereo reconstruction algorithms. Proc IEEE Comput Soc Conf Comput Vision Pattern Recognit. 2006;1:519–26. https://doi.org/10.1109/CVPR.2006.19.
29. Wang X, Wang C, Liu B, et al. Multi-view stereo in the Deep Learning Era: a comprehensive review. Displays. 2021;70(October):102102. https://doi.org/10.1016/j.displa.2021.102102.
30. Zhang Z. A flexible new technique for camera calibration. IEEE Trans Pattern Anal Mach Intell. 2000;22(11):1330–4. https://doi.org/10.1109/34.888718.
31. Hartley R, Zisserman A. Multiple view geometry in computer vision, 2nd edn. Cambridge: Cambridge University Press; 2004.
32. Gonzalez-Huitron V, Ponomaryov V, Ramos-Diaz E, Sadovnychiy S. Parallel framework for dense disparity map estimation using Hamming distance. Signal Image Video Process. 2018;12(2):231–8. https://doi.org/10.1007/s11760-017-1150-3.